Journal of Materials Chemistry A

ROYAL SOCIETY OF CHEMISTRY

PAPER

Cite this: J. Mater. Chem. A, 2022, 10, 4711

Cross-linked structure of self-aligned p-type SnS nanoplates for highly sensitive NO_2 detection at room temperature†

Young Geun Song, ‡[a] In-Hwan Baek,‡[ab] Jae-Gyun Yim,[ac] Taeyong Eom,[d] Taek-Mo Chung, [d] Chul-Ho Lee,[c] Cheol Seong Hwang, [b] Chong-Yun Kang *[ac] and Seong Keun Kim *[ac]

Morphological engineering of two-dimensional chalcogenides has led to significant advances in terms of high responses and low power consumption for chemiresistive gas sensors. Nevertheless, the practical use of such nanostructured two-dimensional materials is still limited. The difficulties in patterning resulting from the morphological complexity of nanostructures and the absence of highly sensitive p-type semiconductor sensors are major obstacles. In this study, we report a highly sensitive NO_2 gas sensor composed of cross-linked p-type SnS nanoplates on SiO_2 nanorods. The area-selective growth of SnS by atomic layer deposition allows for the self-aligned formation of SnS nanoplates only on SiO_2 nanorods without an additional patterning process. The cross-linked structure of the SnS nanoplates enabled the electrical connection of small and very thin SnS nanoplates, which increased the resistance difference between the hole accumulation layer across the entire surface and the less conductive core. Consequently, this cross-linked structure enhances the gas response of p-type semiconductor sensors. The gas response did not vary significantly when the relative humidity (RH) changed from 40% to 80%. Under ambient conditions of 60% RH at room temperature, the SnS sensor exhibited a high response of 116% to 5 ppm NO_2, along with an extremely low detection limit of 21 ppt. The sensor showed excellent selectivity for NO_2, with a minimal response to other gases. This approach provides possibilities for employing p-type semiconductors in practical room-temperature sensor applications.

Received 29th December 2021
Accepted 24th January 2022

DOI: 10.1039/d1ta11014d

rsc.li/materials-a

Introduction

Chemiresistive-type gas sensors have been intensively studied with significant technological advances in collecting and processing data from the surrounding environment.[1–3] These sensors offer real-time information on the presence of hazardous or explosive gases, allowing people to be aware of and manage the environment.[4,5] In general, the gas-sensing process by the adsorption and desorption of gas molecules on the surface of metal oxides requires a high operating temperature of 150–400 °C, which not only consumes significant amounts of power but also degrades the long-term stability.[6,7] Therefore, it is important to implement gas sensors that can operate at room temperature.

Recently, two-dimensional (2D) chalcogenide semiconductors have been considered as promising sensing materials capable of operating at room temperature because of their large surface-to-volume ratio.[8–16] The use of morphological engineering to maximise the surface-to-volume ratio by developing structures such as flower-like nanostructures and vertically aligned flakes has also been proposed to enhance the gas-sensing performance.[13,17–19]

However, such nanostructure strategies of 2D chalcogenides have not been used in practice to realise semiconductor sensors. A challenge in realising 2D chalcogenide gas sensors is to define the sensing area. Vapour deposition techniques generally do not have area selectivity, and they tend to form thin films not only in the desired area but also in undesired peripheral areas. The sensing materials formed on the peripheral areas can provide detour current paths, as shown in Fig. 1(a). In this case, the actual resistance of the sensor may differ from the designed resistance value. Moreover, the presence of sensing material in the peripheral region causes unwanted electrical connections between adjacent sensors in sensor arrays. Therefore, it is important to eliminate the

[a]Electronic Materials Research Center, Korea Institute of Science and Technology, Seoul 02791, South Korea. E-mail: cykang@kist.re.kr; s.k.kim@kist.re.kr

[b]Department of Materials Science and Engineering and Inter-University Semiconductor Research Center, Seoul National University, Seoul 08826, South Korea

[c]KU-KIST Graduate School of Converging Science and Technology, Korea University, Seoul 02841, South Korea

[d]Division of Advanced Materials, Korea Research Institute of Chemical Technology, Daejeon 34114, South Korea

† Electronic supplementary information (ESI) available. See DOI: 10.1039/d1ta11014d

‡ Y. G. S. and I. H. B. contributed equally to this study.

sensing materials formed in the peripheral area. However, it is challenging to fabricate nanostructured materials only on the desired area of the sensor device when the adopted film-growth techniques do not have area selectivity. A top-down approach for nanofabrication, which involves lithographical patterning and etching, is not feasible for the morphological engineering of 2D materials.[20–23] Additionally, nanostructures such as nanoplates and nanorods are highly vulnerable to structural damage during the wet cleaning processes, which are essential in the patterning process.

The absence of highly sensitive p-type semiconductor sensors presents another challenge. Many existing studies have focused on the development of n-type semiconductor sensors. Despite the importance of p-type semiconductor gas sensors,[24,25] the status of research on the implementation of highly sensitive p-type semiconductor gas sensors is still delayed. A challenge for realising highly sensitive p-type 2D chalcogenide gas sensors is the presence of a hole accumulation layer (HAL) across the entire surface due to the adsorption of oxygen from the atmosphere.[26] The chemiresistive variation in the p-type sensor in response to a specific gas is insufficient because the HAL determines the total resistance of the sensors. This is because the presence of the HAL generally decreases the resistance of the sensor material to an extremely low value, which can hardly be increased by the adsorption of other gases. In contrast, in n-type semiconductors, an electron depletion layer is formed across the semiconductor surface. Additionally, the polycrystalline configuration of n-type sensor materials constitutes serial electrical contacts at grain boundaries. In this case, the chemiresistive variation at the intergrain contacts determines the gas response.[24] Therefore, p-type gas sensors with parallel conduction paths have an inherently low gas response compared to n-type gas sensors with serial conduction paths between the grains and intergrain contacts.

NO_2 has major environmental and biological effects, such as acid rain and respiratory diseases.[27] NO_2 can also be used as a biomarker for asthma and gastrointestinal disorders.[28] Thus, the ultrasensitive detection of NO_2 is of considerable importance. SnS is a p-type semiconductor with a layered structure. This material is a good candidate for p-type chemiresistive-type NO_2 sensors because of its high selectivity toward NO_2 and its ability to operate at room temperature.[29,30]

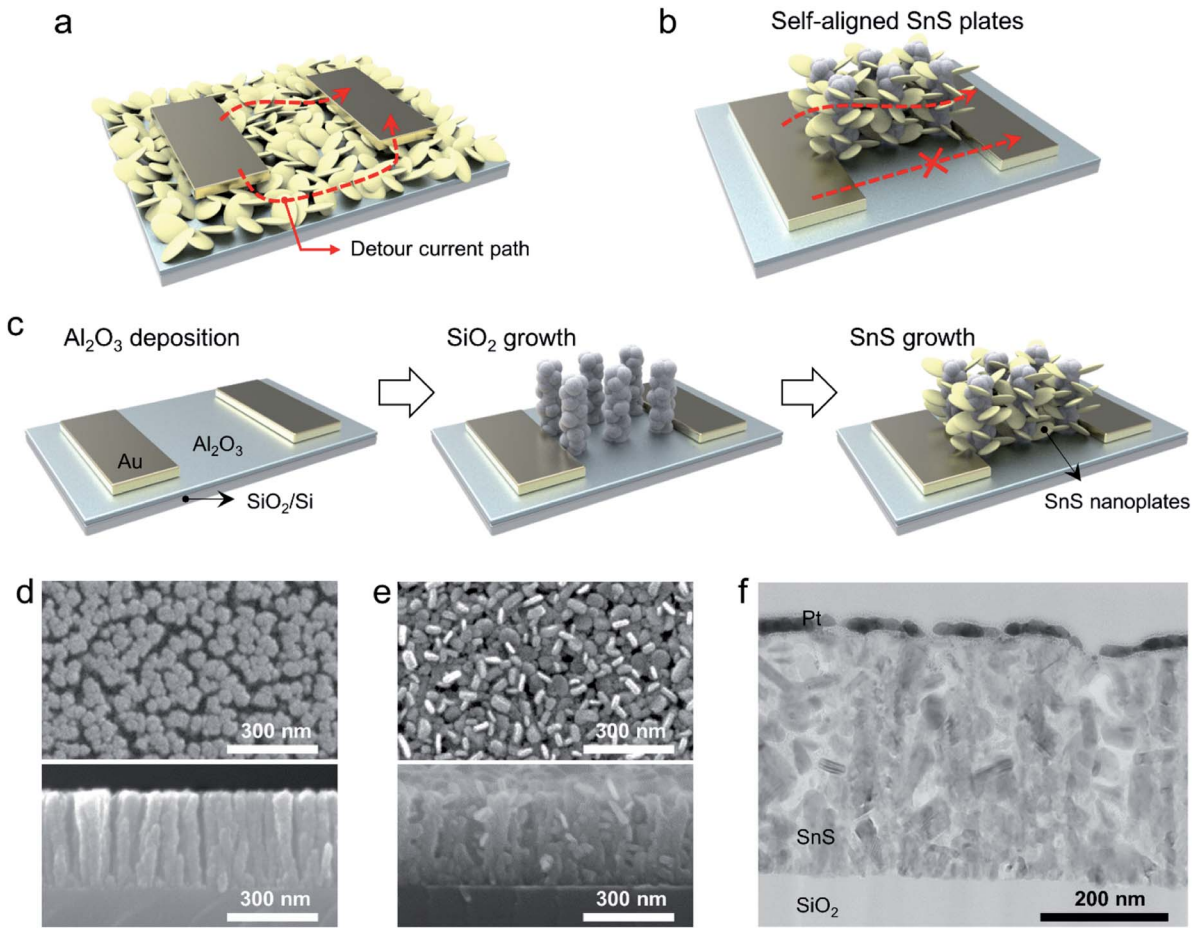

Fig. 1 (a) Schematic of the gas sensor composed of nanostructured materials with detour current paths. (b) Proposed structure of the gas sensor in which crosslinked SnS nanoplates are self-aligned. (c) Illustration of the fabrication process of the self-aligned and crosslinked SnS nanoplates. Plan-view (upper panel) and cross-sectional (lower panel) SEM images of the (d) SiO_2 nanorods and (e) randomly orientated SnS nanoplate-formed nanorods. (f) Cross-sectional TEM image of SnS nanoplates over the SiO_2 nanorods.

In this work, we propose a new structure of crosslinked p-type SnS nanoplates for highly sensitive detection of NO_2 gas at room temperature, as shown in Fig. 1(b). The cross-linked structure of the SnS nanoplates was fabricated on a SiO_2 nanorod template using atomic layer deposition (ALD). The strong substrate-dependent growth behaviour of SnS ALD led to the selective growth of SnS only on the SiO_2 nanorod templates. Therefore, this approach does not require any subsequent patterning processes after SnS formation. Additionally, we figured out that the increase in the resistance of the less conductive core of SnS grains enhanced their response to NO_2. We determined that the cross-linked structure of the p-type SnS nanoplates is very suitable for increasing the resistance of the less conductive core of SnS grains. Given that the ambient atmosphere always contains humidity, we examined the response and selectivity to NO_2 under different humidity conditions at room temperature.

Results and discussion

We previously reported the ALD processing of layer-structured α-SnS from bis(1-dimethylamino-2-methyl-2-propoxy)tin(II) ($Sn(dmamp)_2$) and H_2S,[31–33] where the process led to the evolution of non-continuous layers composed of randomly orientated SnS nanoplates.[31] Such morphology resulted from the strong anisotropic adsorption of the precursors depending on the crystal planes. Hence, the ALD of SnS over three-dimensional (3D) structured templates such as nanorods allows the formation of randomly oriented SnS nanoplates throughout the 3D structure, rather than the conformal coverage commonly expected in ALD. The ALD technique further facilitated crosslinking of the SnS nanoplates by controlling the spacing between the SiO_2 nanorods and the size of the SnS nanoplates.

The proposed sensor structure with self-aligned and cross-linked SnS nanoplates was fabricated as illustrated in Fig. 1(c). The substrate was covered with a 5 nm-thick Al_2O_3 layer. SiO_2 nanorods with approximate heights and diameters of 300 nm and 30 nm, respectively, were formed on the pre-patterned area between the Au electrodes by a glancing angle deposition technique.[34–36] Subsequently, ALD SnS nanoplates were formed by ALD of SnS. The SnS nanoplates were selectively grown on SiO_2 nanorods, even without a specific patterning process. The actual structure of the fabricated sensor was determined by electron microscopy. Fig. 1(d) shows plan-view (upper panel) and cross-sectional (lower panel) scanning electron microscopy (SEM) images of SiO_2 nanorods. The SiO_2 nanorods were vertically aligned. The subsequent SnS ALD process formed randomly oriented SnS nanoplates over the SiO_2 nanorods rather than a continuous film, as shown in Fig. 1(e). The cross-sectional transmission electron microscopy (TEM) image shown in Fig. 1(f) further verifies the uniform distribution of the SnS nanoplates over the entire surface of the SiO_2 nanorods, despite the high aspect ratio of more than ten. The self-limiting behaviour of ALD enables excellent uniformity over nanorods with a high aspect ratio.

Tin sulfides are a family of materials comprising SnS polymorphs of layered orthorhombic α-SnS and cubic π-SnS as well as SnS_2.[37–40] These phases have different reactivities to a specific gas species in terms of resistance change. Hence, the phase purity of the nanoplates formed *via* ALD was examined. Fig. 2(a) shows the X-ray diffraction (XRD) patterns of the SiO_2 nanorods before and after SnS ALD. Although the SiO_2 nanorods were

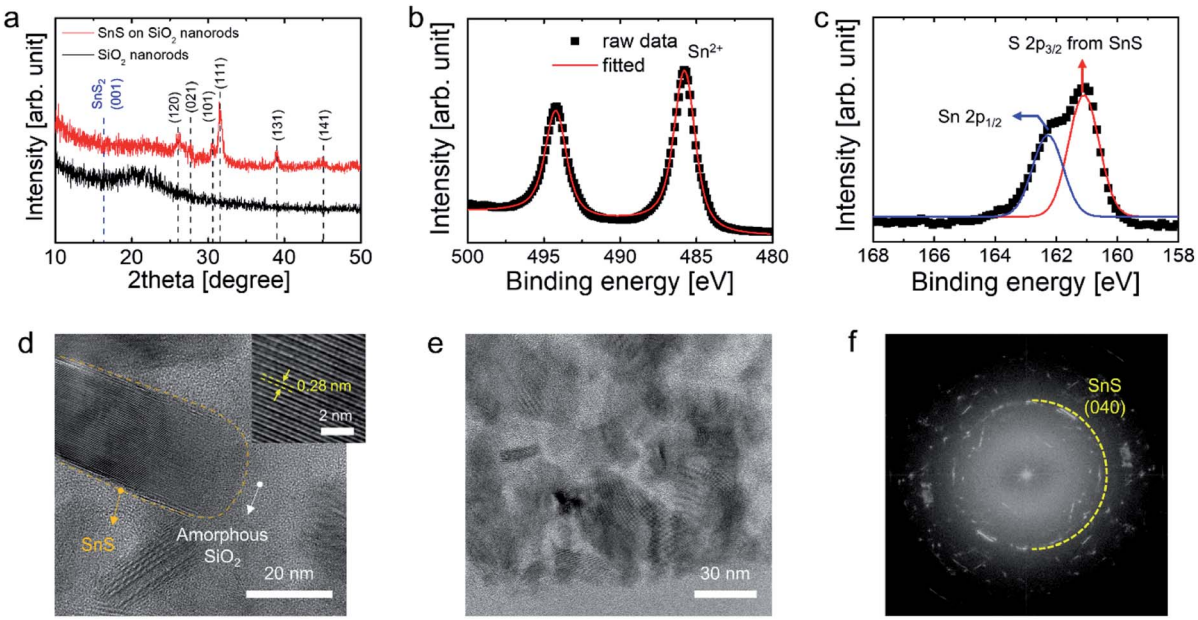

Fig. 2 (a) XRD patterns of SiO_2 nanorods before and after SnS ALD. XPS spectra of (b) Sn 3d and (c) S 2p core levels in the SnS nanoplates grown on SiO_2 nanorods. (d) HRTEM image of the middle part of the SnS-deposited SiO_2 nanorods. (e) HRTEM and (f) fast Fourier transform images of the bottom part of the SnS-deposited nanorods.

amorphous, the ALD-grown layer exhibited only Bragg peaks corresponding to α-SnS. No peaks corresponding to secondary phases such as π-SnS and SnS_2 were observed. Raman analysis on the SnS nanoplates also shows only peaks corresponding to α-SnS (Fig. S1, ESI†), indicating the phase purity of the nanoplates. X-ray photoelectron spectroscopy (XPS) further verified the evolution of single-phase SnS. The XPS profiles of the Sn 3d core level in the structure shown in Fig. 2(b) exhibited a Sn $3d_{5/2}$ single peak at 485.8 eV, corresponding to Sn^{2+} in SnS.[31] The S 2p spectrum shown in Fig. 2(c) also exhibited an S $2p_{3/2}$ single peak at 161.2 eV, which corresponds to S^{2-} in SnS.[31] The other oxidation states were not observed in the XPS profiles, indicating the formation of single-phase SnS. The atomic ratio of Sn : S in the SnS nanoplates was estimated to be 54 : 46 using X-ray fluorescence (Fig. S2, ESI†), which is close to the stoichiometric ratio of SnS.

High-resolution TEM (HRTEM) further confirmed the appearance of nanoplate-shaped SnS grains. Fig. 2(d) shows the HRTEM image of the middle part of the SnS-deposited SiO_2 nanorods. The SnS layer did not fully cover the SiO_2, and SnS grains were sparsely formed on the surface of the amorphous SiO_2 nanorods. The magnified image of the grain shown in Fig. 2(d) verifies the layered structure of orthorhombic SnS from the observation of planes with an interspacing of 0.28 nm, corresponding to the α-SnS (040) planes. Fig. 2(e) and (f) show HRTEM and fast Fourier transform images of the bottom part of the nanorods, respectively. These results demonstrate that plate-shaped grains of α-SnS are sparsely formed, even in the bottom region of the nanorods. This indicated that crosslinking between the SnS nanoplates occurred throughout the nanorods.

The nanostructure of the SnS nanoplates is vulnerable to the common patterning process. We observed that the SnS nanoplates crumbled near the edges after a common wet-cleaning process (Fig. S3, ESI†). This emphasises that a selective growth technique is essential for facilitating the application of nanostructured materials in sensors without patterning of sensing materials. We previously reported the strong substrate-dependent growth of SnS using the same precursors[31] in which SnS growth did not occur on an ALD-grown Al_2O_3 surface, whereas the ALD process on the SiO_2 surface exhibited a linear increase in the amount of SnS as the number of cycles increased without an incubation cycle. We verified this inherent substrate dependence of SnS ALD on two different substrates, ALD-grown Al_2O_3 and e-beam-evaporated SiO_2, which were used to fabricate SnS sensors. The mass gain of SnS did not increase over up to 150 cycles on the Al_2O_3 surface, whereas the growth of SnS was achieved on the evaporated SiO_2 surface with constant growth per cycle, as shown in Fig. 3(a). No deposits were observed on the Al_2O_3 surface after ALD of SnS (Fig. S4, ESI†).

In this study, we attempted the self-aligned growth of SnS on SiO_2 based on inherent substrate-dependent growth. The growth area of SnS is defined by the SiO_2 nanorods formed on the Al_2O_3 surface, as shown in Fig. 1(b). Fig. 3(b) shows the SEM image of the fabricated SnS sensor with an active sensing area of 30 μm × 300 μm between the Au electrodes. The vicinity of the boundary of the active sensing area was observed using SEM. The SEM image shown in Fig. 3(c) shows a sharp interface

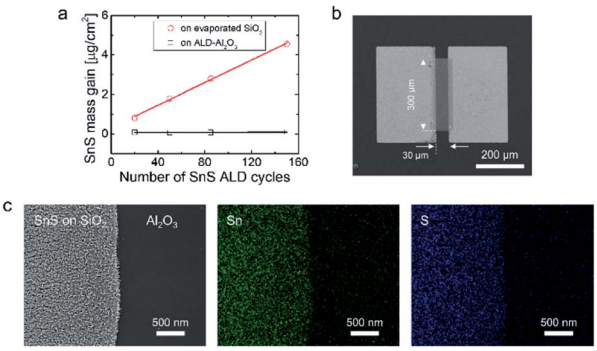

Fig. 3 (a) Variation in the mass gain of SnS grown on ALD-grown Al_2O_3 and e-beam-evaporated SiO_2 substrates as a function of the ALD cycle. (b) SEM image of the fabricated SnS sensor with an active sensing area of 30 μm × 300 μm. (c) SEM image and elemental (Sn and S) mapping of the vicinity of the boundary of the SnS active sensing area.

between the SnS sensing area and Al_2O_3-coated peripheral area. SnS nanoplates selectively developed on the SiO_2 nanorods, whereas no growth occurred on the Al_2O_3 surface. The area-selective growth of SnS was further confirmed from the energy-dispersive X-ray spectroscopy results, in which Sn and S were detected only in the area with the SiO_2 nanorods, as shown in Fig. 3(c).

The response to NO_2 is defined using the following equation:

$$\text{Response [\%]} = [(R_a/R_g - 1) \text{ (for p-type) or } (R_g/R_a - 1) \text{ (for n-type)}] \times 100 \quad (1)$$

where R_a and R_g indicate the resistance of the sensor in the absence and presence of the target gas, respectively. To enhance the response, R_g should change significantly with the flow of NO_2 gas. The R_g values of n-type sensing materials vary significantly upon exposure to NO_2. This is related to the conduction configuration of n-type sensing materials, that is, serial conduction paths between the grains and intergrain contacts, as shown in Fig. 4(a). Upon exposure to NO_2, the electrons were more depleted at the inter-grain contacts. The high resistance at the inter-grain contacts determines the R_g value of the sensor as shown in Fig. 4(a). However, in p-type sensing materials a HAL is formed over the entire surface of p-type materials under ambient conditions, where hole carriers are even more accumulated upon exposure to NO_2.[41] The parallel competition between the more-conductive HAL and the less-conductive core region determines the conduction in p-type materials, as shown in Fig. 4(a). Hence, the R_g value changes less in p-type sensing materials, indicating the inherently low response of the p-type semiconductor sensors.

We considered eqn (1) to enhance the response of p-type SnS sensors to NO_2. Considering the equivalent resistance diagram for a p-type SnS sensor – a parallel connection of a low-resistance HAL and a less conductive core – shown in Fig. 4(b), the response of the p-type SnS sensor can be expressed using the following equation:

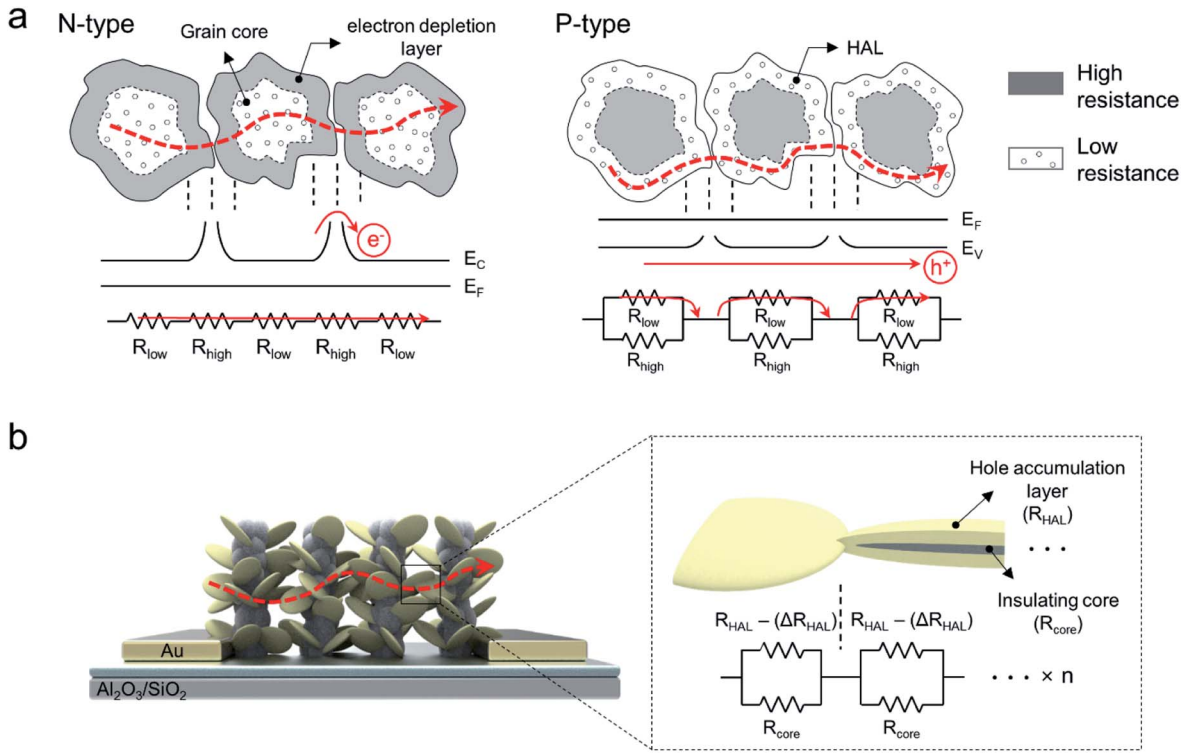

Fig. 4 (a) Equivalent circuits of n-type and p-type semiconductor sensors. (b) Mechanism of the increase in response in the cross-linked structure of SnS nanoplates.

$$\text{Response } [\%] = \left(\frac{R_a}{R_g} - 1\right) = \frac{1}{\left(\frac{R_{HAL}}{\Delta R_{HAL}} - 1\right)\left(1 + \frac{R_{HAL}}{R_{core}}\right)} \quad (2)$$

where R_{core} denotes the resistance of the less conductive core, and R_{HAL} and ΔR_{HAL} indicate the resistance of the HAL in the absence of NO_2 and the change in the resistance in the presence of NO_2, respectively (Fig. 4(b)). More details on the development of eqn (2) are provided in Note S1 in the ESI.† According to the equation, both the R_{HAL}/R_{core} and $R_{HAL}/\Delta R_{HAL}$ ratios should decrease to enhance the response. Among the two ratios, the $R_{HAL}/\Delta R_{HAL}$ value was mainly determined by the number of NO_2 molecules adsorbed on the surface. Therefore, it is imperative to reduce the R_{HAL}/R_{core} value to enhance the response of p-type SnS sensors to NO_2.

An effective way to decrease the R_{HAL}/R_{core} value is to reduce the thickness of the SnS nanoplates. This is because R_{core} is inversely proportional to the thickness, whereas R_{HAL} is independent of thickness. However, it is well known that the formation of a thin continuous SnS film is difficult.[31,32,42] Generally, the formation of a continuous SnS film for electrical connections inevitably involves an increase in the thickness. From this viewpoint, the cross-linked structure proposed in this study is an effective way to increase R_{core}. As shown in Fig. 1(d), the distance between the SiO_2 nanorods in the proposed structure is only tens of nanometres, and an electrical connection is possible even with very thin and small SnS nanoplates. This configuration allows high R_{core} owing to the electrical connection of thinner SnS grains, as shown in Fig. 4(b).

The number of SnS ALD cycles determines the size and thickness of the SnS nanoplates. Hence, R_{core} of the SnS nanoplates was mainly affected by the number of SnS ALD cycles. Accordingly, we examined the NO_2 response of the SnS sensor with respect to the number of SnS ALD cycles. Fig. 5(a) shows the variation in the base resistance, that is, the R_a value of the sensors with SnS nanoplates on SiO_2 nanorods, as a function of the number of ALD cycles. The R_a of the fabricated SnS structure was affected by the resistance of the SnS grains and the number of crosslinking points. Note that R_a is invariant to the applied voltage. Excellent linearity in the *I–V* characteristics was confirmed (Fig. S5, ESI†). The R_a values were obtained after exposure to dry air at room temperature. The variation in the R_a value of SnS grown on the planar surface of an e-beam-evaporated SiO_2 film is shown in Fig. 5(a). The R_a value of the fabricated SnS sensor decreased as the number of ALD cycles increased. Furthermore, the R_a value of the fabricated sensors was measurable after only 70 ALD cycles, whereas the R_a value of the SnS layer formed on the planar SiO_2 was not measurable for up to 600 cycles. This indicates that the SnS grains were electrically connected between adjacent SiO_2 nanorods over 70 ALD cycles. Additionally, the SEM images of SnS formed on the SiO_2 nanorods shown in Fig. 5(b) indicate the connection of the grains, even in short ALD cycles (Fig. 5(b) and S6, ESI†), whereas SnS grown on planar SiO_2 for the same number of ALD cycles had isolated grains (Fig. S7, ESI†). This implies that the proposed cross-linked structure achieved a high R_{core} that could not be obtained in a planar SnS film structure.

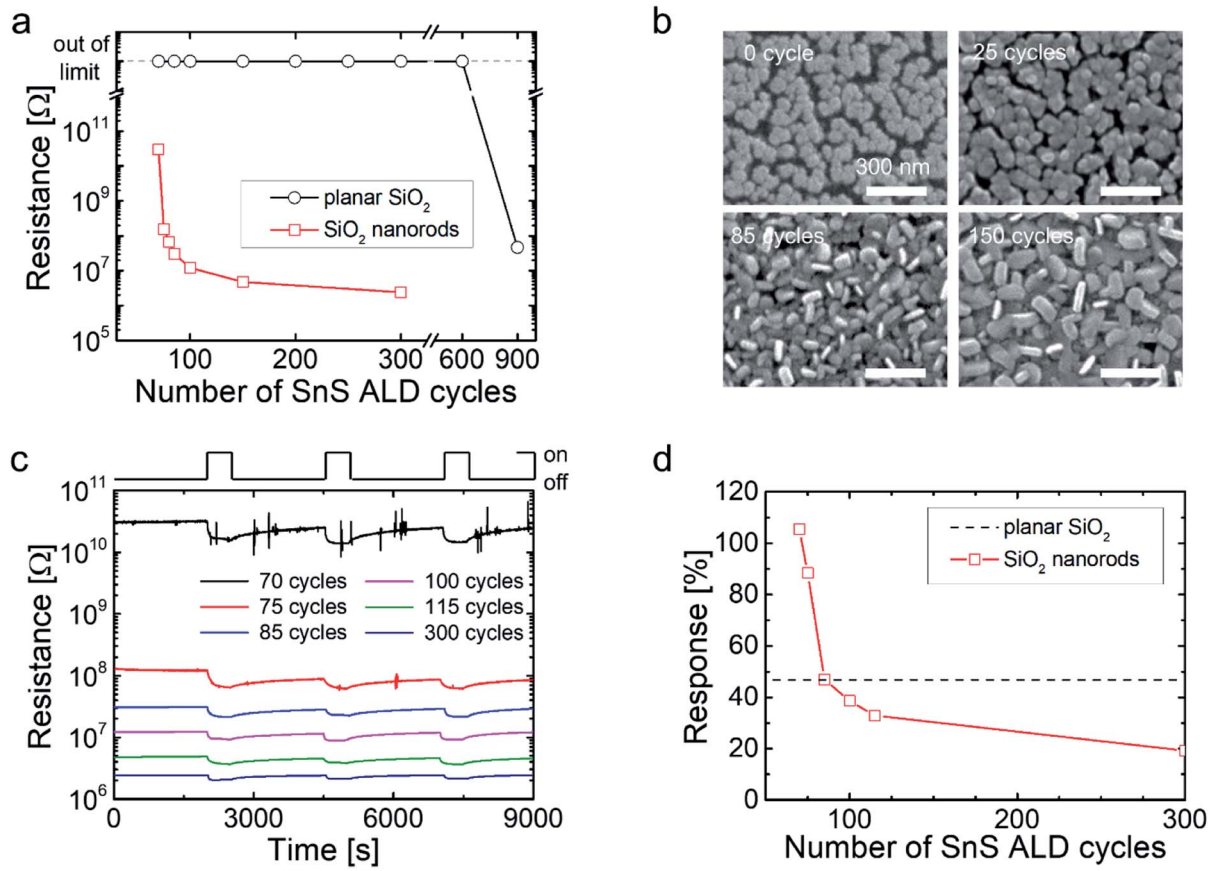

Fig. 5 (a) Variation in the resistance of SnS grown on SiO_2 nanorods and on planar SiO_2 as a function of the ALD cycle at room temperature under exposure to dry air. (b) SEM images of SnS grown on SiO_2 nanorods for 0, 25, 85, and 150 ALD cycles. (c) Variation in the resistance of the devices with SnS grown for 70, 75, 85, 100, 115, and 300 cycles under pulses of 5 ppm NO_2. (d) Variation in the response of the SnS sensors to 5 ppm NO_2 as a function of the ALD cycle.

Fig. 5(c) shows the variation in the resistance of the fabricated SnS devices with the number of ALD cycles under pulses of 5 ppm NO_2 at room temperature. The gas-sensing mechanism of SnS based on resistive change can be understood as physisorption-based charge transfer. The resistance of the devices decreased upon exposure to NO_2 and recovered after the NO_2 gas pulse was halted. This is a typical p-type semiconducting behaviour, representing the p-type nature of the ALD-grown SnS. The physisorption of NO_2 molecules onto SnS transferred electrons from SnS to NO_2.[30,41] The charge transfer is equivalent to hole doping into SnS, increasing the conductivity.[30] To understand the change in the response values in terms of the base resistance, the variation in the response to 5 ppm NO_2 as a function of the number of ALD cycles is illustrated in Fig. 5(d). As expected, the response to 5 ppm NO_2 increased as the number of ALD cycles decreased; that is, an increase in R_{core} enhanced the response to NO_2. In particular, the response of the crosslinked structure of SnS grown for 70 cycles is more than double that of the planar SnS film structure. The variation in the resistance of the planar SnS film structure is also shown in Fig. S8 in the ESI.† This supports the idea that the configuration of the crosslinked SnS nanoplates effectively improves the response of the p-type semiconductor gas sensor.

We examined the gas-sensing properties of the crosslinked SnS sensor under humid conditions because moisture is always present in the environment where such sensors operate. The presence of humidity not only enhanced the response value but also reduced the response and recovery times (Fig. S9, ESI†), and the response did not significantly change in the relative humidity (RH) range from 40% to 80%. Therefore, we examined the response at room temperature and 60% RH in terms of NO_2 concentration. Fig. 6(a) shows the variation in the resistance of SnS grown for 75 ALD cycles under pulses of NO_2 gas at concentrations ranging from 0.1 to 20 ppm in 60% RH. The resistance was abruptly reduced by the pulse of NO_2 gas, and it recovered after NO_2 injection was halted. Furthermore, we observed a decrease in resistance with increasing NO_2 concentration. As shown in Fig. 6(b), the response calculated from the change in resistance showed excellent linearity with the NO_2 concentration. The limit of detection, which is defined as 3 × standard deviation of the base response/slope (0.496 ppm^{-1}) of the graph shown in Fig. 6(b), is extremely low at 21 ppt. This sub-ppb-level detection limit and excellent linearity of the response demonstrate the ability of the proposed SnS sensor to accurately and reliably estimate the NO_2 gas concentration under ambient conditions. The resistance of the SnS sensor

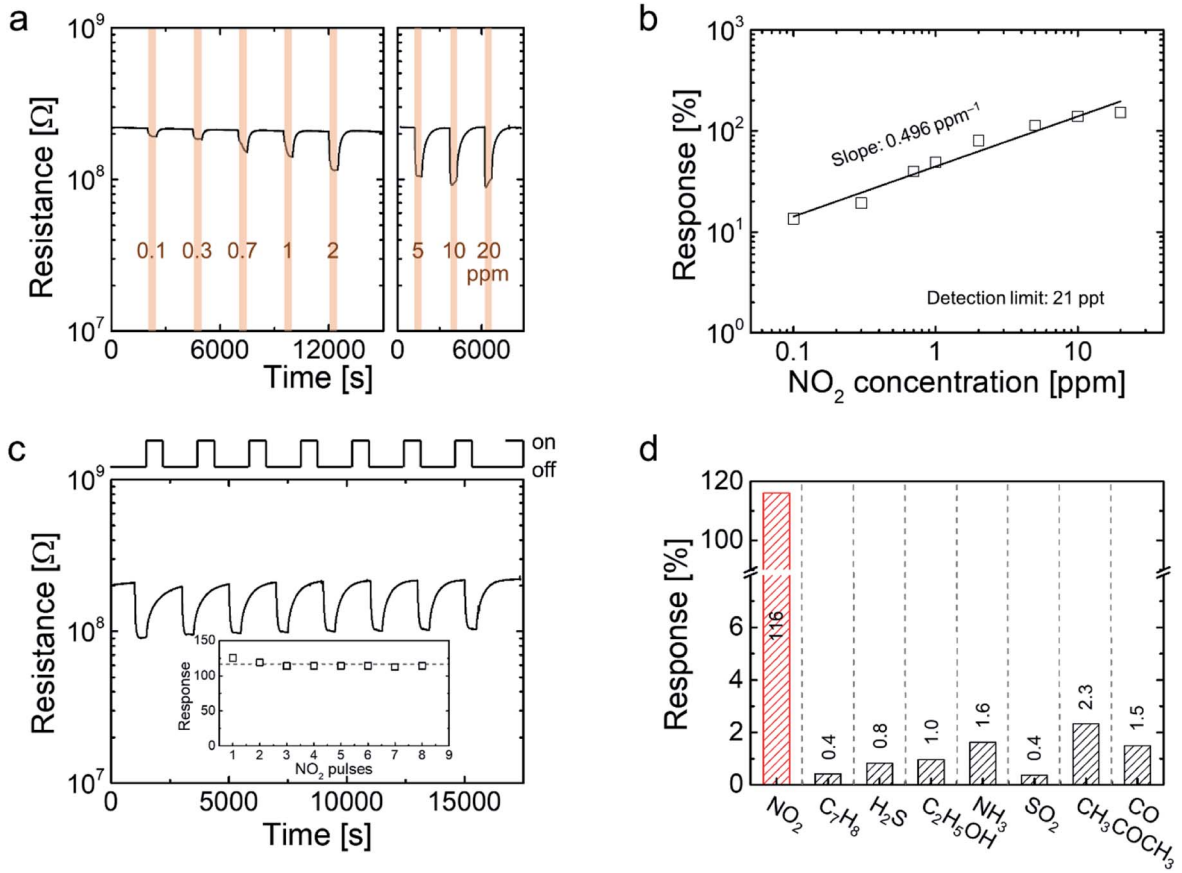

Fig. 6 (a) Variation in the resistance of the SnS sensor under pulses of NO_2 gas at concentrations ranging from 0.1 to 20 ppm. (b) Variation in the response to NO_2 gas as a function of NO_2 concentration. (c) Variation in the resistance of the SnS sensor under eight consecutive pulses of 5 ppm NO_2. (d) Response comparison of the SnS sensor toward various gases (NO_2, C_7H_8, H_2S, C_2H_5OH, NH_3, SO_2, CH_3COOCH_3, and CO) with a concentration of 5 ppm. All measurements shown in the figure were performed at room temperature under 60% RH.

changed reproducibly after eight consecutive pulses of NO_2 at 5 ppm and 60% RH at room temperature, as shown in Fig. 6(c). The average response rate was 116%. The reproducible response was further verified by a small standard deviation of only 3.48%, as shown in the inset of Fig. 6(c), which indicates the chemical stability of the SnS nanoplates. The excellent device-to-device uniformity of the fabricated SnS sensors was also verified from the measurements of the base resistance and NO_2 response on multiple devices (Fig. S10, ESI†). We further examined the stability of SnS nanoplates upon exposure to NO_2. Even after exposure of the SnS sensor to 100 ppm NO_2 for 5 min, irreversible changes, such as the variation in the valence states of Sn^{2+} ions or loss of S ions due to oxidation, were not observed (Fig. S11, ESI†).

Table 1 Comparison of NO_2 sensing performance of the previously reported gas sensors using p-type 2D materials. All the data were obtained at room temperature

Material	Structure	Response (concentration)	Detection limit	Ref.
SnS	Cross-linking of nanoplates	116% (5 ppm)	21 ppt	This work
SnS	Thin crystals	60% (1 ppm)	<100 ppb	29
WS_2	Nanosheets	68.4% (5 ppm)	100 ppb	41
WS_2	1D nanostructures	30% (1 ppm)	13.726 ppb	45
WS_2	Hierarchical fibers	49% (10 ppm)	<1 ppm	46
MoS_2	Multilayers	97% (25 ppm)	—	47
MoS_2	Multilayers	10.8% (10 ppm)	<1 ppm	48
$MoSe_2$	Nanosheets	40% (5 ppm)	—	49
MoS_2	Thin layers	54% (100 ppm)	—	50
MoS_2	Nanowires	18.1% (5 ppm)	4.6 ppb	51
MoS_2	Vertically aligned	10% (100 ppm)	—	18
MoS_2	Nanoflowers	67.4% (10 ppm)	84 ppb	52

The gas selectivity of the fabricated SnS sensor was explored based on the changes in response to various reactive gases. Fig. 6(d) shows the response values upon exposure to NO_2, C_7H_8, H_2S, C_2H_5OH, NH_3, SO_2, CH_3COCH_3, and CO at 60% RH and room temperature. The concentrations of all gases were fixed at 5 ppm. The variation in the response to all gases is shown in Fig. S12 in the ESI.† The SnS sensor exhibited a high response only for NO_2 and negligible responses for other gases, confirming the excellent selectivity of the SnS sensor toward NO_2. It was reported from first-principles calculations that the adsorption energy of NO_2 on SnS is larger than that of other gases, such as CO, CO_2, NH_3, SO_2, and H_2S, and the charge transfer between SnS and the adsorbed molecule is also larger for NO_2 than for other gases.[30,43,44] Thus, the excellent selectivity of SnS toward NO_2 can be understood as a result of the easy adsorption of NO_2 on SnS and the large charge transfer.

The NO_2 sensing performances of the other p-type semiconductor sensors using 2D materials are summarized in Table 1.[18,29,41,45–52] The p-type semiconductor sensors generally exhibited a relatively low response to NO_2 and a high limit of detection. Compared with the other p-type semiconductor sensors, the crosslinked structure of the SnS nanoplates displayed a superior sensing performance with a high response and an ultralow detection limit.

Conclusions

In this study, we fabricated a highly sensitive p-type SnS gas sensor that operates at room temperature. The opposite growth behaviour of SnS ALD on SiO_2 and Al_2O_3 resulted in the selective formation of SnS nanoplates only on the SiO_2 nanorod template, even with no additional patterning process. The vertically aligned SnS nanoplates grown on the SiO_2 nanorods facilitated cross-linking of the SnS nanoplates. This unique structure effectively reduced the R_{HAL}/R_{core} ratio of the SnS nanoplates, which enhanced the gas response to NO_2. Under humid conditions, the SnS gas sensor is highly selective for NO_2, with minimal responses to other gases. It also showed excellent linearity in terms of NO_2 concentration, exhibiting an extremely low detection limit of 21 ppt. We believe that our findings will provide new insights into the implementation of highly sensitive p-type semiconductor gas sensors. Furthermore, the area-selective growth technique can relieve patterning issues of nanostructured sensing materials.

Experimental

Fabrication of SnS gas sensors

A 5 nm-thick Al_2O_3 layer was deposited by ALD on a SiO_2/Si substrate. Au/Ti electrodes with an area of 400 μm × 200 μm and a spacing of 30 μm were fabricated on the substrate using photolithography and a lift-off process. To deposit the SiO_2 thin film and nanorods, e-beam evaporation of SiO_2 was performed at a rotation speed of 12 rpm and glancing angles of 0° and 80°. The detailed procedure for the fabrication of the nanorods has been previously reported.[34–36] SnS was deposited in a travelling wave-type chamber by ALD from $Sn(dmamp)_2$ and H_2S. ALD was performed at 240 °C under a nominal working pressure of 1 Torr. The ALD cycle consisted of Sn precursor feeding for 2 s, purging for 10 s, S precursor feeding for 2 s, and purging for 20 s. The details of the ALD process for SnS can be found in our previous reports.[31,32]

Characterisation

Field-emission SEM (Inspect F, FEI) and TEM (TitanTM80-300, FEI) were used to investigate the morphology and crystal structure of the sensing materials. The chemical states of the materials were examined using XPS (PHI 5000 VersaProbe, Ulvac-PHI) with a monochromatic Al Kα X-ray source (1486.6 eV). Wavelength dispersive X-ray fluorescence (ZSX Primus II, Rigaku) was used to determine the mass gain and stoichiometry of SnS. The crystal structure and crystallinity were examined using XRD (ATX-G, Rigaku).

Gas sensor measurements

The gas sensing performance of the SnS gas sensors was examined in a quartz tube (diameter, 3 cm; length, 30 cm) at 25 °C with a constant flow rate of 1000 sccm. Dry air (80% N_2 and 20% O_2) was used as the balancing gas. The concentration of the target gas was calibrated by mixing it with a balanced gas using a mass flow controller. The sensor resistance was measured at a DC voltage of 0.5 V using a source measurement unit (2401 source metre; Keithley).

Conflicts of interest

There are no conflicts to declare.

Acknowledgements

The authors gratefully acknowledge the support of the National Research Foundation of Korea grant (2021M3D1A2045626) and the National Research Council of Science & Technology (NST) grant by the Korean government (MSIP) (No. CAP-17-04-KRISS), the Energy Technology Development Project (KETEP) grant funded by the Ministry of Trade, Industry and Energy, Republic of Korea (2018201010636A), the Korea Institute of Science and Technology (2E31771), and the KU-KIST Graduate School of Converging Science and Technology Program.

References

1 Y. K. Jo, S.-Y. Jeong, Y. K. Moon, Y.-M. Jo, J.-W. Yoon and J.-H. Lee, *Nat. Commun.*, 2021, **12**, 1–9.
2 C. Park, W. T. Koo, S. Chong, H. Shin, Y. H. Kim, H. J. Cho, J. S. Jang, D. H. Kim, J. Lee and S. Park, *Adv. Mater.*, 2021, 2101216.
3 X. Geng, S. Li, L. Mawella-Vithanage, T. Ma, M. Kilani, B. Wang, L. Ma, C. C. Hewa-Rahinduwage, A. Shafikova and E. Nikolla, *Nat. Commun.*, 2021, **12**, 1–11.
4 K.-D. Kang, L. Chen, H. Yi, B. Wang and M. Sha, *Big Data Cogn. Comput.*, 2017, **1**, 5.

5 S. Y. Jeong, J. S. Kim and J. H. Lee, *Adv. Mater.*, 2020, **32**, 2002075.
6 J. Zhang, X. Liu, G. Neri and N. Pinna, *Adv. Mater.*, 2016, **28**, 795–831.
7 N. Joshi, T. Hayasaka, Y. Liu, H. Liu, O. N. Oliveira and L. Lin, *Microchim. Acta*, 2018, **185**, 1–16.
8 A. Azizi, M. Dogan, H. Long, J. D. Cain, K. Lee, R. Eskandari, A. Varieschi, E. C. Glazer, M. L. Cohen and A. Zettl, *Nano Lett.*, 2020, **20**, 6120–6127.
9 S. Yang, C. Jiang and S.-h. Wei, *Appl. Phys. Rev.*, 2017, **4**, 021304.
10 J. Ping, Z. Fan, M. Sindoro, Y. Ying and H. Zhang, *Adv. Funct. Mater.*, 2017, **27**, 1605817.
11 J. J. Pyeon, I.-H. Baek, Y. G. Song, G. S. Kim, A.-J. Cho, G.-Y. Lee, J. H. Han, T.-M. Chung, C. S. Hwang, C.-Y. Kang and S. K. Kim, *J. Mater. Chem. C*, 2020, **8**, 11874–11881.
12 Y. Qin, Z. Wei and Y. Bai, *Vacuum*, 2021, **183**, 109792.
13 Z. Yang, C. Su, S. Wang, Y. Han, X. Chen, S. Xu, Z. Zhou, N. Hu, Y. Su and M. Zeng, *Nanotechnology*, 2020, **31**, 075501.
14 X. Chen, T. Wang, J. Shi, W. Lv, Y. Han, M. Zeng, J. Yang, N. Hu, Y. Su and H. Wei, *Nano-Micro Lett.*, 2022, **14**, 1–15.
15 Q. Sun, Z. Gong, Y. Zhang, J. Hao, S. Zheng, W. Lu, Y. Cui, L. Liu and Y. Wang, *J. Hazard. Mater.*, 2022, **421**, 126816.
16 E. Wu, Y. Xie, B. Yuan, H. Zhang, X. Hu, J. Liu and D. Zhang, *ACS Sens.*, 2018, **3**, 1719–1726.
17 W. Yan, W. Yan, T. Chen, J. Xu, Q. Tian and D. Ho, *ACS Appl. Nano Mater.*, 2020, **3**, 2545–2553.
18 S.-Y. Cho, S. J. Kim, Y. Lee, J.-S. Kim, W.-B. Jung, H.-W. Yoo, J. Kim and H.-T. Jung, *ACS Nano*, 2015, **9**, 9314–9321.
19 W. T. Koo, J. H. Cha, J. W. Jung, S. J. Choi, J. S. Jang, D. H. Kim and I. D. Kim, *Adv. Funct. Mater.*, 2018, **28**, 1802575.
20 E. Rani and L. S. Wong, *Adv. Mater. Technol.*, 2019, **4**, 1900181.
21 M. G. Stanford, P. D. Rack and D. Jariwala, *npj 2D Mater. Appl.*, 2018, **2**, 1–15.
22 R. Ionescu, A. George, I. Ruiz, Z. Favors, Z. Mutlu, C. Liu, K. Ahmed, R. Wu, J. S. Jeong and L. Zavala, *Chem. Commun.*, 2014, **50**, 11226–11229.
23 M. Amani, M. L. Chin, A. L. Mazzoni, R. A. Burke, S. Najmaei, P. M. Ajayan, J. Lou and M. Dubey, *Appl. Phys. Lett.*, 2014, **104**, 203506.
24 H.-J. Kim and J.-H. Lee, *Sens. Actuators, B*, 2014, **192**, 607–627.
25 T. P. Mokoena, H. C. Swart and D. E. Motaung, *J. Alloy Compd.*, 2019, **805**, 267–294.
26 L. Zhang, K. Khan, J. Zou, H. Zhang and Y. Li, *Adv. Mater. Interfaces*, 2019, **6**, 1901329.
27 K. Belanger, J. F. Gent, E. W. Triche, M. B. Bracken and B. P. Leaderer, *Am. J. Respir. Crit. Care Med.*, 2006, **173**, 297–303.
28 C. Wang and P. Sahay, *Sensors*, 2009, **9**, 8230–8262.
29 J. Wang, G. Lian, Z. Xu, C. Fu, Z. Lin, L. Li, Q. Wang, D. Cui and C.-P. Wong, *ACS Appl. Mater. Inter.*, 2016, **8**, 9545–9551.
30 F.-F. Hu, H.-Y. Tang, C.-J. Tan, H.-Y. Ye, X.-P. Chen and G.-Q. Zhang, *IEEE Electron Device Lett.*, 2017, **38**, 983–986.
31 I.-H. Baek, J. J. Pyeon, Y. G. Song, T.-M. Chung, H.-R. Kim, S.-H. Baek, J.-S. Kim, C.-Y. Kang, J.-W. Choi, C. S. Hwang, J. H. Han and S. K. Kim, *Chem. Mater.*, 2017, **29**, 8100–8110.
32 I.-H. Baek, A.-J. Cho, S. Kim, G. Y. Lee, J. H. Han, T.-M. Chung, S.-H. Baek, C.-Y. Kang, J.-S. Kim, C. S. Hwang and S. K. Kim, *Chem. Mater.*, 2020, **32**, 9026–9033.
33 I.-H. Baek, J. J. Pyeon, G.-Y. Lee, Y. G. Song, H. Lee, S. O. Won, J. H. Han, C.-Y. Kang, T.-M. Chung, C. S. Hwang and S. K. Kim, *Chem. Mater.*, 2020, **32**, 2313–2320.
34 Y. G. Song, J. Y. Park, J. M. Suh, Y.-S. Shim, S. Y. Yi, H. W. Jang, S. Kim, J. M. Yuk, B.-K. Ju and C.-Y. Kang, *Chem. Mater.*, 2018, **31**, 207–215.
35 Y. G. Song, I. Jung, J. Shin, Y.-S. Shim, G. S. Kim, B.-K. Ju and C.-Y. Kang, *Sens. Actuators, B*, 2021, **332**, 129481.
36 Y. G. Song, Y. S. Shim, J. M. Suh, M. S. Noh, G. S. Kim, K. S. Choi, B. Jeong, S. Kim, H. W. Jang and B. K. Ju, *Small*, 2019, **15**, 1902065.
37 R. E. Abutbul, E. Segev, L. Zeiri, V. Ezersky, G. Makov and Y. Golan, *RSC Adv.*, 2016, **6**, 5848–5855.
38 R. Abutbul, A. Garcia-Angelmo, Z. Burshtein, M. Nair, P. Nair and Y. Golan, *CrystEngComm*, 2016, **18**, 5188–5194.
39 A. Rabkin, S. Samuha, R. E. Abutbul, V. Ezersky, L. Meshi and Y. Golan, *Nano Lett.*, 2015, **15**, 2174–2179.
40 O. V. Bilousov, Y. Ren, T. Törndahl, O. Donzel-Gargand, T. Ericson, C. Platzer-Björkman, M. Edoff and C. Hägglund, *Chem. Mater.*, 2017, **29**, 2969–2978.
41 T. Xu, Y. Liu, Y. Pei, Y. Chen, Z. Jiang, Z. Shi, J. Xu, D. Wu, Y. Tian and X. Li, *Sens. Actuators, B*, 2018, **259**, 789–796.
42 J.-H. Ahn, M.-J. Lee, H. Heo, J. H. Sung, K. Kim, H. Hwang and M.-H. Jo, *Nano Lett.*, 2015, **15**, 3703–3708.
43 A. Shukla and N. Gaur, *Phys. E*, 2020, **120**, 114054.
44 A. Shukla and N. Gaur, *Phys. B*, 2019, **572**, 12–17.
45 J. M. Suh, K. C. Kwon, T. H. Lee, C. Kim, C. W. Lee, Y. G. Song, M.-J. Choi, S. Choi, S. H. Cho and S. Kim, *Sens. Actuators, B*, 2021, **333**, 129566.
46 D.-H. Youn, B.-J. Kim and S. J. Yun, *Nanotechnology*, 2019, **31**, 105602.
47 Y. Zhao, J.-G. Song, G. H. Ryu, K. Y. Ko, W. J. Woo, Y. Kim, D. Kim, J. H. Lim, S. Lee, Z. Lee, J. Park and H. Kim, *Nanoscale*, 2018, **10**, 9338–9345.
48 T. Xu, Y. Pei, Y. Liu, D. Wu, Z. Shi, J. Xu, Y. Tian and X. Li, *J. Alloy Compd.*, 2017, **725**, 253–259.
49 S. Zhang, T. H. Nguyen, W. Zhang, Y. Park and W. Yang, *Appl. Phys. Lett.*, 2017, **111**, 161603.
50 D. J. Late, Y.-K. Huang, B. Liu, J. Acharya, S. N. Shirodkar, J. Luo, A. Yan, D. Charles, U. V. Waghmare and V. P. Dravid, *ACS Nano*, 2013, **7**, 4879–4891.
51 R. Kumar, N. Goel and M. Kumar, *Appl. Phys. Lett.*, 2018, **112**, 053502.
52 N. T. Thang, N. H. Thoan, C. M. Hung, N. Van Duy, N. Van Hieu and N. D. Hoa, *RSC Adv.*, 2020, **10**, 12759–12771.